

# Review: Overcoming the paradox of strength and ductility in ultrafine-grained materials at low temperatures

Praveen Kumar<sup>1</sup> · Megumi Kawasaki<sup>2,3</sup> · Terence G. Langdon<sup>3,4</sup>

Received: 23 April 2015 / Accepted: 30 May 2015 / Published online: 17 June 2015  
© Springer Science+Business Media New York 2015

**Abstract** Ultrafine-grained (UFG) materials with grain sizes in the submicrometer or nanometer range may be prepared through the application of severe plastic deformation (SPD) to bulk coarse-grained solids. These materials generally exhibit high strength but only very limited ductility in low-temperature testing, thereby giving rise to the so-called paradox of strength and ductility. This paradox is examined and a new quantitative diagram is presented which permits the easy insertion of experimental data. It is shown that relatively simple procedures are available for achieving both high strength and high ductility in UFG materials including processing the material to a very high strain and/or applying a very short-term anneal immediately after the SPD processing. Significant evidence is now available demonstrating the occurrence of grain boundary sliding in these materials at low temperatures, where this is attributed to the presence of non-equilibrium grain boundaries and the occurrence of enhanced diffusion along these boundaries.

## Introduction

It is now well established that the grain size is an exceptionally important, and perhaps the dominant, structural parameter in polycrystalline metals. At low temperatures, typically at temperatures up to  $\sim 0.5T_m$  where  $T_m$  is the absolute melting temperature, the measured yield stress,  $\sigma_y$ , varies with the grain size,  $d$ , through the Hall–Petch relationship which is given by [1, 2],

$$\sigma_y = \sigma_o + k_y d^{-1/2} \quad (1)$$

where  $\sigma_o$  is the lattice friction stress and  $k_y$  is a yielding constant. It follows from Eq. (1) that a reduction in grain size leads to an increase in the overall strength. Accordingly, thermo-mechanical processing operations are used regularly in industry in order to produce significant grain refinement. Nevertheless, the grain sizes produced by these procedures are typically of the order of a few micrometers and it has proven generally impossible to reduce the grains to within the submicrometer range.

This situation changed in 1988 with the demonstration that much smaller grains, lying within the submicrometer range, may be produced through the application of severe plastic deformation (SPD) to bulk coarse-grained solids [3]. Specifically, it was demonstrated that the application of SPD processing to an Al–4 % Cu–0.5 % Zr alloy reduced the grain size to  $\sim 0.3 \mu\text{m}$  thereby giving both high strength and superplastic properties. Following this report, a world-wide interest developed, and has continued to the present day, in using SPD processing in order to achieve ultrafine-grained (UFG) materials with average grain sizes in the submicrometer or even the nanometer range.

The fundamental principle of SPD processing is that a very high strain is imposed on the material without introducing any significant change in the overall dimensions of

---

✉ Terence G. Langdon  
langdon@usc.edu

<sup>1</sup> Department of Materials Engineering, Indian Institute of Science, Bangalore 560012, India

<sup>2</sup> Division of Materials Science and Engineering, Hanyang University, Seoul 133-791, South Korea

<sup>3</sup> Departments of Aerospace & Mechanical Engineering and Materials Science, University of Southern California, Los Angeles, CA 90089-1453, USA

<sup>4</sup> Materials Research Group, Faculty of Engineering and the Environment, University of Southampton, Southampton SO17 1BJ, UK

the sample. This means in practice conventional metal processing techniques, such as extrusion, rolling, and drawing, are necessarily excluded. Nevertheless, various SPD techniques are now available and they have been summarized and analyzed in several recent reviews [4–8]. To date, most interest has centered on the two SPD techniques of equal-channel angular pressing (ECAP) and high-pressure torsion (HPT) [9–11], primarily because ECAP is relatively easy to conduct in any mechanical testing laboratory and HPT, by comparison with ECAP, produces materials having both smaller grain sizes [12, 13] and a higher fraction of high-angle grain boundaries [14]. In ECAP the material is in the form of a rod or bar and it is pressed through a die constrained within a channel bent through a sharp angle [15] whereas in HPT the sample is in the form of a thin disk and it is subjected to a high pressure and concurrent torsional straining [16].

A critical development arising early in the processing of these UFG metals was that the materials exhibit high strength but only very limited ductility. This led to the so-called *paradox of strength and ductility* [17] which is appropriately summarized by the maxim that “materials may be strong or ductile, but rarely both at once” [18, 19]. This loss in ductility at very small grain sizes is due to the low rate of strain hardening in these materials combined with the low value for the strain rate sensitivity,  $m$ . Thus, when the rate of strain hardening is high, dislocations accumulate within the grains and, combined with a high value of  $m$ , the onset of necking is delayed so that the materials are able to exhibit reasonable levels of tensile ductility. This behavior contrasts with UFG metals where the very small grains interfere with the easy storage of dislocations and instead the dislocations are absorbed at the grain boundaries so that the rate of strain hardening is low and the materials achieve only limited elongations to failure [20–22].

The classic paradox of strength and ductility was first represented by the schematic illustration shown in Fig. 1 where the yield stress is plotted against the elongation to failure and almost all UFG metals lie in the shaded area below the solid curve [17]. This plot shows representative datum points for Al and Cu where the numbers next to the lines denote the strains imposed during rolling and the original plot also includes points for other materials such as Co, Mg, and Ti. Also shown in Fig. 1 are two points labeled nano Ti and nano Cu where these nanostructured metals exhibit combinations of exceptional strength and ductility after processing through 5 turns of HPT and 16 passes of ECAP, respectively. It was concluded from these limited results that it may be feasible to achieve both high strength and good ductility in UFG metals by processing through SPD to very large strains and thereby increasing the strain rate sensitivity leading to the occurrence of grain

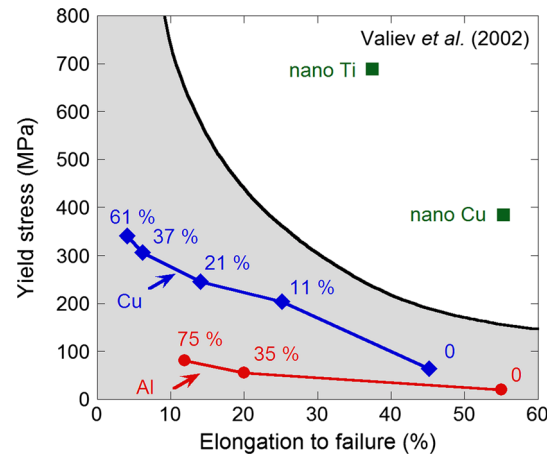


**Fig. 1** Conventional plot of yield stress against elongation to failure illustrating the paradox of strength and ductility: almost all UFG metals lie in the shaded area below the *solid curve* but the two points labeled nano Ti and nano Cu are exceptions to the rule where nanostructures were achieved by using SPD processing to impose very large strains [17]

boundary sliding (GBS) [17]. This conclusion presents an intriguing possibility which is examined in more detail in the following sections.

## Achieving a combination of high strength and good ductility

### Effect of processing to very high strains

Several different strategies have been proposed for achieving both high strength and good ductility in UFG metals [20, 23–32] but often these strategies are applicable only under limited conditions: for example, in precipitation-hardened alloys [25] or in materials containing high densities of nanotwins [32]. Accordingly, it is appropriate to examine the possibility of achieving high strength and good ductility by conducting conventional SPD processing to very high strains.

The standard illustration of the strength-ductility paradox in Fig. 1 is qualitative in nature because there is no definitive relationship delineating the solid curve which separates high strength and high ductility in the upper part of the diagram from conventional materials in the lower part. Furthermore, Fig. 1 shows the absolute value of the elongation to failure but this is known to be affected by the gauge length to thickness ratio wherein a tensile specimen with small gauge length to thickness ratio may artificially show a very high elongation to failure [33, 34]. Accordingly, it is first necessary to establish an alternative illustration for the strength-ductility paradox.

As described in detail in an earlier report [35], the flow characteristics may be conveniently represented by plotting the normalized yield stress, given by  $YS_{\text{UFG}}/YS_{\text{CG}}$ , against the normalized elongation to failure, given by  $\epsilon_{\text{fl-UFG}}/\epsilon_{\text{fl-CG}}$ , where CG denotes the same material having a coarse grain size. The principle of this type of plot is shown in Fig. 2 where the dashed horizontal and vertical lines depict the situations where  $YS_{\text{UFG}}/YS_{\text{CG}}$  and  $\epsilon_{\text{fl-UFG}}/\epsilon_{\text{fl-CG}}$  are both equal to 1.0. Any experimental points lying in the shaded areas to the left of, and/or below, the dashed lines will correspond to conventional behavior where either the strength or the ductility is inferior to the CG material. Alternatively, points lying in the open area in the upper right of the diagram correspond to the high strength-high ductility (HSHD) condition and this represents the region where the paradox of strength and ductility breaks down. It is interesting to note that the approach of plotting normalized stress against normalized ductility minimizes the inherent uncertainties that arise when comparing the ductilities of samples having different gauge lengths. This is because each of the datum point in Fig. 2 is normalized with respect to a reference sample of the same geometry and this minimizes the artificial effects that arise from differences in the gauge length to sample thickness ratio.

It is important to recognize two points with respect to Fig. 2. First, this plot is equivalent to the conventional qualitative depiction in Fig. 1 except that it now becomes feasible to insert quantitative information directly onto the diagram. Second, and as shown earlier [35], other similar and equally effective representations are also feasible by plotting the ultimate tensile strength, given by  $UTS_{\text{UFG}}$

, or the normalized uniform elongation, given by  $\epsilon_{\text{uniform-UFG}}/\epsilon_{\text{uniform-CG}}$ .

In order to check the feasibility of overcoming the strength-ductility paradox by imposing a very high strain, experiments were conducted on a cast Al–7 % Si hypoeutectic alloy where the material was processed by HPT through different numbers of turns,  $N$ , under an imposed pressure of 6.0 GPa at room temperature (298 K) using an anvil rotation rate of 1 rpm [35]. Miniature tensile specimens were machined from the HPT disks after processing and then pulled to failure at 298 K using an initial strain rate of  $1.0 \times 10^{-3} \text{ s}^{-1}$ . Representative stress–strain curves are shown in Fig. 3 for the as-cast condition and for samples processed by HPT through 1/4, 1, 5, and 10 turns, respectively. Inspection of Fig. 3 shows that all stress–strain curves are essentially similar with small regions of strain hardening upon yielding and then, beyond the UTS, extensive strain softening to failure. The values of the YS and UTS are consistently higher after processing by HPT, even for the specimen processed through only 1/4 turn, and the highest elongations to failure are achieved when the samples are processed through the highest values of five and ten turns.

The results in Fig. 3 are similar to those obtained when testing at 298 K at other strain rates in the range from  $1.0 \times 10^{-4}$  to  $1.0 \times 10^{-2} \text{ s}^{-1}$  and the datum points for all strain rates and each specimen are plotted in Fig. 4 [35] using the new quantitative depiction of the yield stress versus elongation to failure as shown earlier in Fig. 2. It is now apparent that some specimens fall to the left of the vertical dashed line so that the elongations are not sufficiently high by comparison with the as-cast material whereas other datum points fall in the HSHD region and these specimens represent a clear breakdown in the

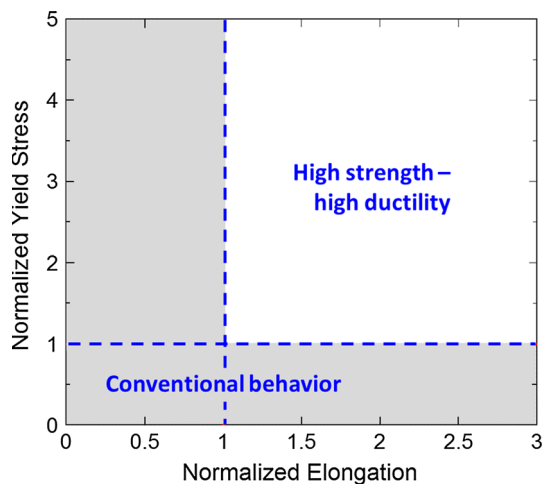


**Fig. 2** A quantitative and simple representation of the paradox of strength and ductility where the normalized yield stress is plotted against the normalized elongation: experimental points lying in the shaded areas exhibit conventional behavior with strength and/or ductility inferior to the coarse-grained material and points lying in the open area at upper right exhibit both high strength and high ductility

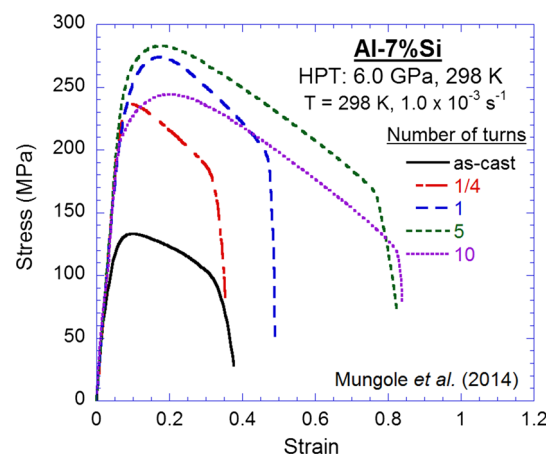


**Fig. 3** Representative plots of engineering stress versus engineering strain for an Al–7 % Si alloy tested at 298 K with an initial strain rate of  $1.0 \times 10^{-3} \text{ s}^{-1}$  [35]: the gauge lengths and thicknesses of all tensile specimens were 0.67 and 1 mm, respectively

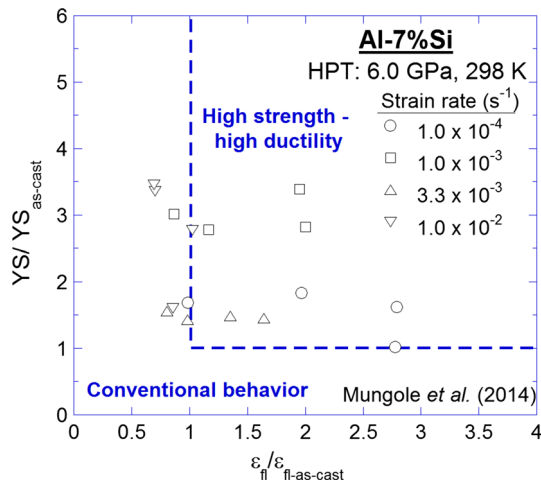


**Fig. 4** Using the quantitative representation of strength and ductility shown in Fig. 2 to illustrate datum points from a number of stress-strain curves for the Al-7 % Si alloy tested at 298 K over a range of initial strain rates from  $1.0 \times 10^{-4}$  to  $1.0 \times 10^{-2} s^{-1}$ : points lying in the region at upper right show combinations of high strength and high ductility which effectively overcomes the paradox of strength and ductility [35]

conventional strength-ductility paradox. It was shown in an earlier report that essentially the same information may be obtained when plotting either the UTS or the uniform elongation for each specimen [35]. However, it should be noted that the instances of transitions to the HSHD region are slightly reduced if the abscissa of Fig. 4 is replaced by the normalized uniform strain [35]. This means, therefore, that an increase in the numbers of turns in HPT produces a clear transition to high strength and high ductility.

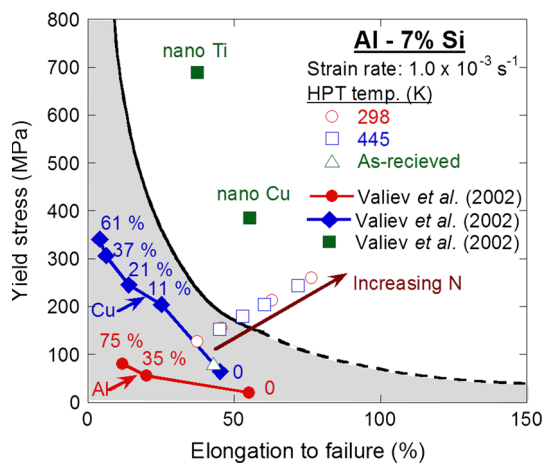


**Fig. 5** Using the conventional plot in Fig. 1 [17] to illustrate experimental datum points for the Al-7 % Si alloy when testing at an initial strain rate of  $1.0 \times 10^{-3} s^{-1}$  after processing by HPT at 298 and 445 K: the arrow shows the effect of increasing the numbers of turns in HPT [35]

The results from these experiments with the Al-7 % Si alloy may be plotted directly onto the strength-ductility diagram as shown in Fig. 1. The result is given in Fig. 5 where the open triangle represents the initial as-cast condition and the open circles and squares show experimental points for the aluminum alloy when testing at an initial strain rate of  $1.0 \times 10^{-3} s^{-1}$  at HPT processing temperatures of 298 and 445 K, respectively: the solid arrow superimposed on Fig. 5 shows the effect of increasing the numbers of turns in HPT [35]. Thus, it can be seen that the Al-7 % Si alloy is significantly stronger than the high-purity UFG aluminum shown in Fig. 1 [17] and, in addition, the strength and ductility are both increased by imposing larger strains in the SPD processing. In practice, these results show that the increase in ductility in the Al-7 % Si alloy is more rapid than the increase in strength. Nevertheless it is readily apparent that HPT processing to high strains provides the capability of simultaneously achieving both high strength and high ductility.

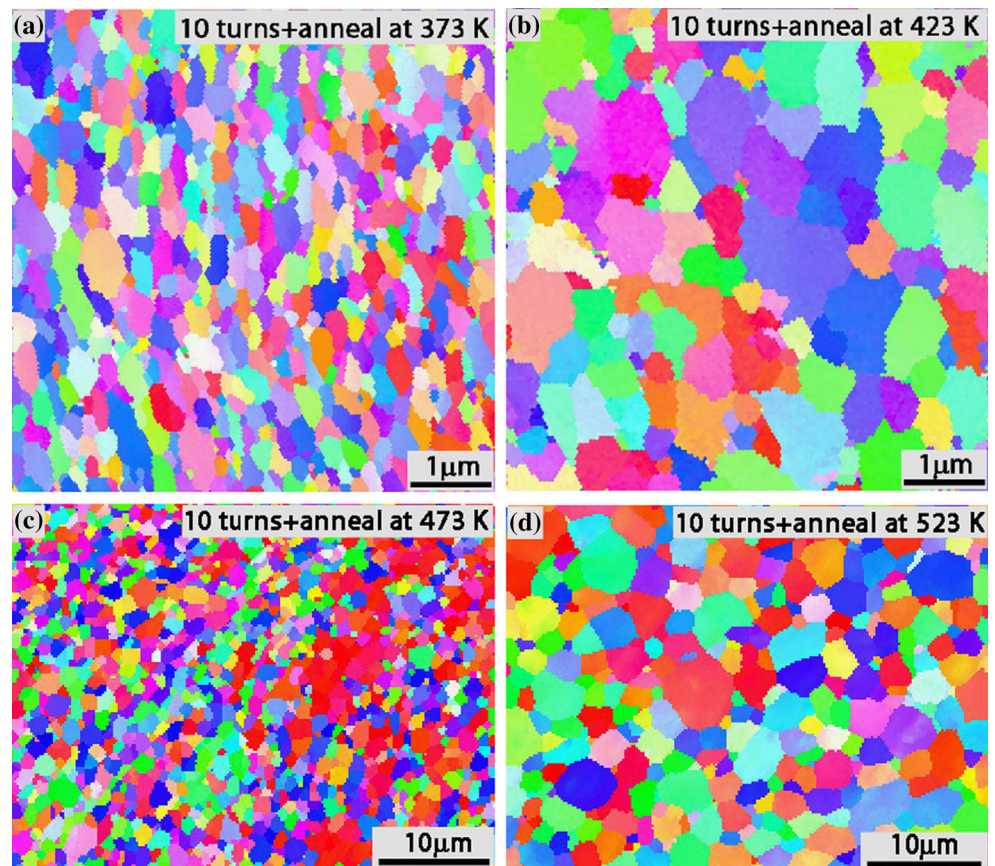
#### Effect of a short-term anneal after processing

As noted earlier, several of the strategies for overcoming the strength-ductility paradox are restricted to a limited range of materials involving nano-twinning or precipitation hardening. However, it was shown in an early report on the processing of Ti by HPT that it is possible to improve the overall ductility by subjecting a material to a very short-term anneal after the SPD processing [36]. The rationale behind this approach is that the short-term annealing produces an ordering of the defect structures within the grain boundaries so that they become more equilibrated without the occurrence of any significant grain growth. In addition, annealing may also decrease the dislocation density in the grain interior of an SPD-processed material, thereby facilitating effective dislocation storage, and an enhanced storage capability may increase the strain hardening leading to increased ductility in these materials. Subsequently, similar results were reported for Cu processed by ECAP [37], Ti processed by ECAP and drawing [38], Ti processed by ECAP-Conform and drawing [39], and pure Ta processed by HPT [40].

As an example of this approach, it is interesting to consider recent results reported for an Al-1.0 % Mg solid solution alloy where the processing was conducted by HPT and the disks were subjected to short-term anneals of 10 min immediately following the HPT processing [41]. The annealed grain size of this alloy was  $\sim 400 \mu m$  prior to HPT processing. However, this was reduced to  $\sim 200 nm$  with a high fraction of high-angle grain boundaries through processing by HPT for ten turns at room temperature under an applied pressure of 6.0 GPa and with a rotation speed of 1 rpm. Following HPT, samples were annealed for 10 min at selected temperatures from 373 to 523 K. Figure 6



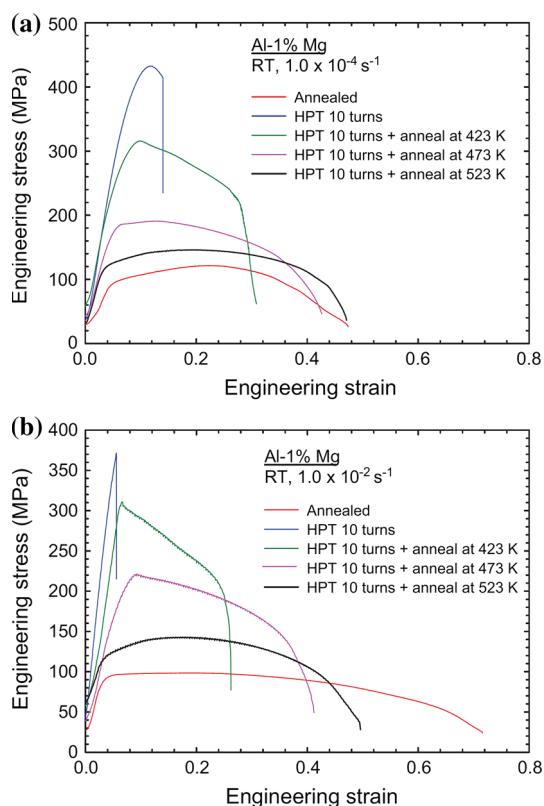
**Fig. 6** Microstructures in an Al–1 % Mg alloy after processing by HPT through ten turns and then annealing for 10 min at **a** 373, **b** 423, **c** 473, and **d** 523 K [41]



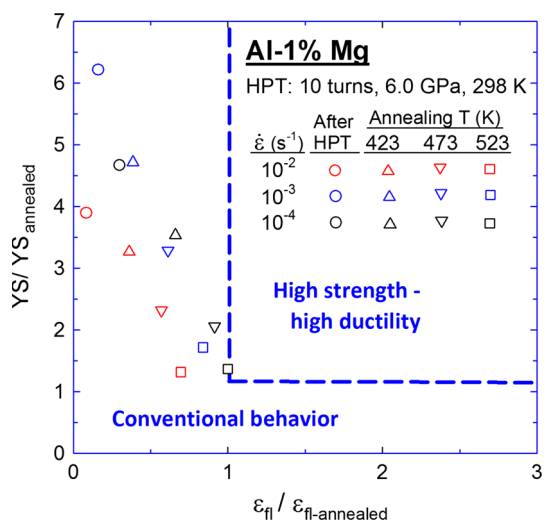
shows representative microstructures after processing through 10 turns and then annealing for 10 min at (a) 373, (b) 423, (c) 473, and (d) 523 K [41]. It is readily apparent from these images that there is little or no grain growth at 373 K but the grains grow to  $\sim 360$  nm at 423 K,  $\sim 940$  nm at 473 K and  $\sim 1.98$   $\mu\text{m}$  at 523 K.

Figure 7 shows representative plots of engineering stress against engineering strain for tensile tests conducted at room temperature using initial strain rates of (a)  $1.0 \times 10^{-4}$  and (b)  $1.0 \times 10^{-2} \text{ s}^{-1}$  [41]. Thus, the unprocessed annealed material consistently exhibits the lowest flow stresses and the largest elongations to failure. For samples processed by ten turns without post-HPT annealing, the stresses are high but the elongations to failure are very small. Nevertheless, the introduction of a short-term anneal at 423, 473 or 523 K gives lower stress levels but much higher ductilities. In general, these results suggest that a short-term post-HPT annealing treatment at a temperature of 423 K appears to represent the optimum condition for achieving both a reasonable level of strength combined with a good tensile ductility.

Figure 8 summarizes the yield stress and elongation to failure data of the Al–1 % Mg alloy as shown in Fig. 7 and now presented in the form of Fig. 2: this plot also includes experimental results for a strain rate of  $1.0 \times 10^{-3} \text{ s}^{-1}$  which are not recorded in Fig. 7. It is apparent from inspection of Fig. 8 that, irrespective of the strain rate, the elongations to failure increase with the severity of the annealing but at the same time the strength also decreases. Nevertheless, although the short-term anneal increases the ductility and alleviates the shortcoming of an essentially brittle behavior after SPD processing, the datum points in Fig. 8 are not displaced into the HSHD region. However, a careful examination of Fig. 8 shows that the elongation to failure of the processed material relative to the unprocessed material increases more at the lowest strain rate of  $10^{-4} \text{ s}^{-1}$  and, furthermore, the decrease in yield stress relative to the increase in ductility is minimum when the sample is annealed at the lowest temperature of 423 K. These observations suggest that a very short-term anneal of the SPD-processed material at low temperatures followed by tensile testing at very low strain rates may be effective in moving the datum points into the HSHD region.



**Fig. 7** Representative stress–strain curves for an Al-1 % Mg alloy in the annealed condition, after processing by HPT and after processing by HPT and then annealing for 10 min at 423, 473 or 523 K: results are shown for initial strain rates of **a**  $1.0 \times 10^{-4}$  and **b**  $1.0 \times 10^{-2} \text{ s}^{-1}$  [41]



**Fig. 8** Quantitative summary of yield stress versus elongation to failure as documented in Fig. 7 and now presented in the form of Fig. 2: the yield stress and elongation to failure data are normalized with respect to the annealed condition

## The role of GBS at these very low temperatures

### Evidence for GBS in UFG materials

As described previously, Figs. 4 and 5 show clearly a transition from the conventional behavior of high strength and low ductility to HSHD for UFG metals processed through SPD to very high strains. It should be noted that the nano Cu and UFG Al-7 % Si samples lying in the HSHD region of Figs. 4 and 5 were tested at room temperature [17, 35] whereas the nano Ti was tested at 523 K ( $\sim 0.27T_m$ ) [17]. Such an increase in the ductilities of UFG materials often occurs simultaneously with an increase in the strain rate sensitivity [35, 42]. Therefore, it is reasonable to anticipate that the increase in ductility and the transition to HSHD may be associated with a different flow mechanism such as the occurrence of GBS at low temperatures [17, 19, 35, 42]. Nevertheless, GBS is a diffusion-controlled process and hence it is generally considered as a significant deformation mechanism only at temperatures greater than or equal to  $\sim 0.5T_m$  [43–46]. It follows, therefore, that GBS is not expected at the relatively low temperatures associated with the transition from conventional behavior to HSHD but in practice there is direct evidence for the occurrence of GBS at low temperatures in these SPD-processed UFG materials. This evidence is now examined.

Examples of GBS were first presented using micro-indentation on the metallographically polished surfaces of UFG samples of high-purity Al [47, 48]. An example is shown in Fig. 9 which depicts the formation of material pileup due to an indentation at room temperature [47]. This sample was processed through 8 passes of ECAP and the resultant grain size was  $\sim 1.2 \mu\text{m}$ . Although material pileup is expected around an indentation, the inset in Fig. 9 also reveals the formation of steps at grain boundaries which is a characteristic feature of GBS. Thus, Fig. 9 provides direct evidence for the occurrence of GBS at a low temperature in a UFG material processed through SPD.

Confirmation for the occurrence of GBS was presented recently in additional experiments conducted on high-purity Al after processing by ECAP. Figure 10 shows a tilted view of a trench fabricated through focused ion beam (FIB) milling in an aluminum sample tested in tension [49, 50]. As schematically depicted in Fig. 10a, GBS leads to the formation of a sharp step at the upper surface of a tested sample and examples of GBS-induced surface steps are marked by arrows in Fig. 10 thereby confirming the occurrence of GBS in the SPD-processed Al at room temperature. These experimental observations support the importance of GBS in enhancing low temperature ductility in SPD-processed UFG materials as well as providing an

**Fig. 9** An AFM scan showing material pileup near the indentation on a metallographically polished surface of UFG high-purity Al; the lines labeled ECAP-1 and ECAP-2 denote two directions where line profiles were generated to measure the GBS steps in the material pileup and the inset shows a magnified view along line ECAP-1 [47]

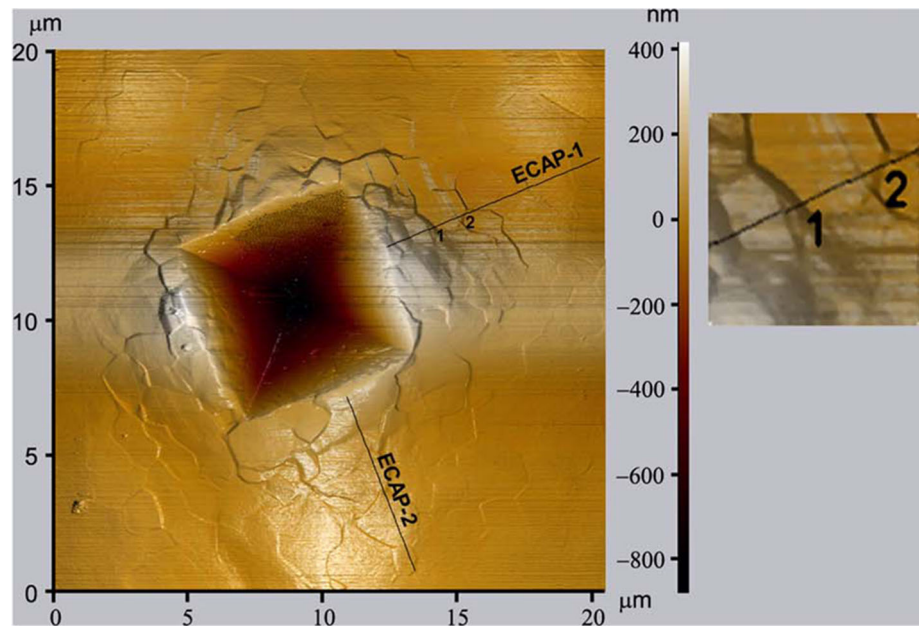
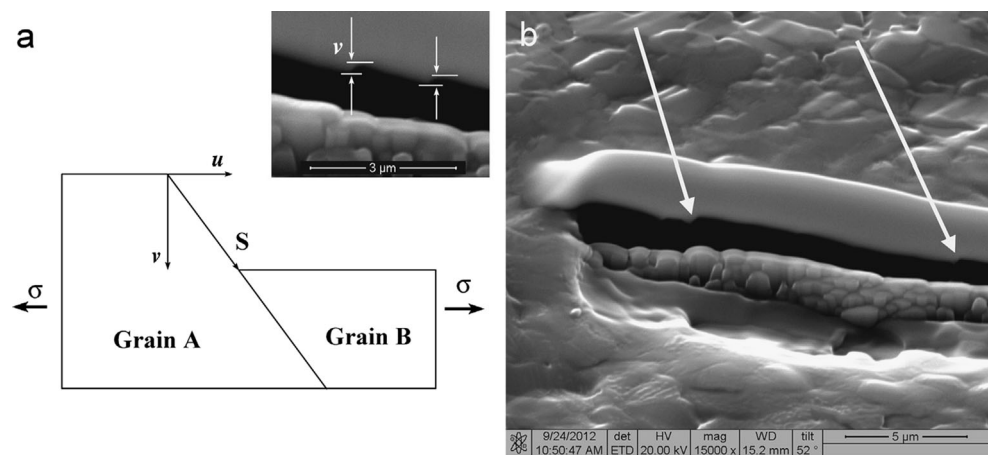


**Fig. 10 a** A profile view schematically showing the relative positions of two grains after GBS, and the inset shows a tilted view of a trench milled into a deformed UFG sample of Al and the method for determining the GBS vertical offset  $v$  on the surface; **b** a cross-sectional view of the trench showing GBS at the locations indicated by solid arrows [49]



explanation for the transition from conventional behavior to HSHD.

The Al sample shown in Fig. 9 had a grain size of  $\sim 1.2 \mu\text{m}$  [47] but it is important to note that this is orders of magnitude larger than the grain sizes used in the early molecular dynamic simulations which provided the first theoretical predictions for the occurrence of GBS in nanocrystalline (NC) materials [51–53]. Thus, it appears initially that the observations of GBS in UFG materials at low temperatures, as demonstrated in Figs. 9 and 10, may be anomalous.

The primary reason for the apparent anomalous occurrence of GBS at low temperatures in these SPD-processed UFG materials lies in the presence of a large volume of non-equilibrium grain boundaries [19, 54–57]. These non-equilibrium boundaries contain an excess of extrinsic

dislocations giving a more distorted structure, a higher energy, a larger free volume, and generally a higher dislocation density than in normal grain boundaries in CG or annealed materials [57]. In practice, it is also clear that the excessive straining during SPD processing leads readily to the formation of these non-equilibrium grain boundaries [19, 54, 57].

Strain mapping analysis based on transmission electron microscopy has shown that these non-equilibrium grain boundaries are significantly wider than normal grain boundaries [57, 58] and this is consistent with early observations by high-resolution electron microscopy of excess dislocations lying in narrow zones close to the boundaries [56]. In addition, due to the high energy and the large free volume or vacancy concentration associated with these non-equilibrium boundaries, diffusion along the



boundaries is significantly faster than in normal boundaries [59–61]. Due to the higher diffusivity, wider grain boundary width, and the overall larger numbers of grain boundaries in UFG materials produced through SPD processing, the material transport through these grain boundaries is expected to be significantly higher than in conventional materials. It follows, therefore, that this extraordinary and unique feature of SPD-processed UFG materials, together with the presence of large fractions of high-angle grain boundaries, are generally considered responsible for the relatively easy occurrence of GBS at low temperatures [19].

### Experimental procedures for measuring GBS in UFG materials

Figure 11 schematically illustrates the occurrence of stress-induced GBS at a pair of adjacent grains where (a) and (b) depict the initial and the final configurations of the grains, respectively [62]. Thus, as shown in Fig. 10, GBS results in an abrupt discontinuity in a straight line drawn parallel to the applied stress at the boundary between the two sliding grains. In principle, an offset in a marker line perpendicular to the applied stress is representative of the GBS vector and the magnitude of this offset may be used to estimate the sliding contribution [63, 64].

As shown in Fig. 11, two types of marker lines may be placed on a metallographically polished surface of a test specimen. The first on the top surface of the sample registers the horizontal offset,  $w_i$ , at a grain boundary as given in the top view of Fig. 11b and the second on the side surface registers a vertical offset,  $v_i$ , due to GBS as shown in the side view of Fig. 11b. In the absence of internal markers, the offset  $v_i$  is equal to the step formed at the top

surface,  $v_j$ , as shown in the side view in Fig. 11b. The first type of offset is easily observed under a scanning electron microscope (SEM) [65, 66] and the second type of offset may be measured using a surface profilometer such as an atomic force microscope (AFM) [62, 67–69] or by milling a trench using FIB followed by observations with SEM [49, 50].

In practice, numerous readings of  $w_i$  or  $v_j$  are taken at consecutive grain boundaries using a set of marker lines or milled cross sections and the average values of  $w_i$  and  $v_i$  are then calculated as  $\langle w \rangle$  and  $\langle v \rangle$ , respectively. Although the magnitudes of the  $v_i$  offsets are dependent upon the precise nature of the surface configuration [64], in practice either parameter may be used to directly measure the strain due to GBS,  $\varepsilon_{\text{gbs}}$ , through the relationships [63]

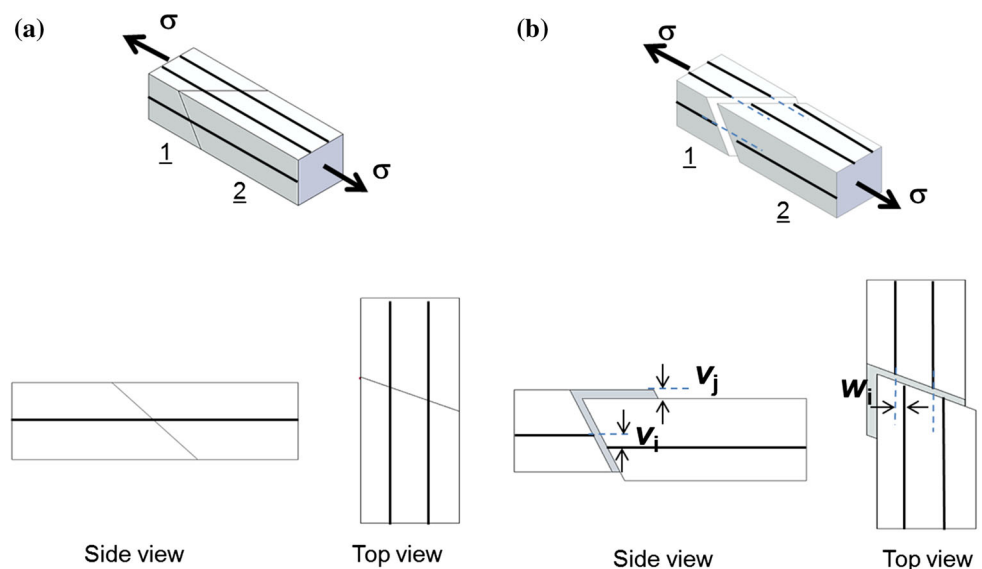
$$\varepsilon_{\text{gbs}} = \phi_1 \frac{\langle w \rangle}{\bar{L}} = \phi_2 \frac{\langle v \rangle}{\bar{L}}, \quad (2)$$

where  $\phi_1$  and  $\phi_2$  are constants which are generally set equal to 1.5 [64, 70] and  $\bar{L}$  is the mean intercept length of the grains. Furthermore, the contribution of  $\varepsilon_{\text{gbs}}$  to the total strain,  $\varepsilon_t$ , defined as  $\xi$ , is then determined as

$$\xi = \frac{\varepsilon_{\text{gbs}}}{\varepsilon_t}. \quad (3)$$

For NC or UFG materials, where the grain sizes and hence the expected GBS offsets are much smaller than in conventional materials, it is often extremely difficult to use marker line methods to measure the offsets  $w_i$  or  $v_i$  and hence it is generally not easy to determine the magnitude of  $\xi$ . For a determination of GBS using  $v_j$ , it is first necessary to prepare an excellent metallographically polished surface and secondly it is important to recognize that the offset measurements are dependent upon the surface topography

**Fig. 11** Schematic illustrations in isometric and side and top views showing the configurations of two neighboring grains, 1 and 2, **a** before and **b** after GBS in response to an applied axial stress: the bold lines represent marker lines drawn parallel to the applied stress which incur sharp offsets at grain boundaries equal to  $v_i$  and  $w_i$  on the side and top surfaces, respectively, due to the occurrence of GBS [62]





at the grain boundaries. In practice, it is feasible to use AFM or SEM to measure  $v_j$  with the high accuracy that is needed in order to measure the very small offsets in NC and UFG materials [62, 67, 69, 71–73].

It was shown very recently that surface profiling using AFM in the non-contact mode is highly effective for measuring  $v_j$  and producing overall topographic profiles of the type shown schematically in Fig. 12 for the Al–7 % Si alloy [62]. The main advantage of conducting AFM scans in the non-contact mode is the simultaneous generation of amplitude error maps which are sensitive to changes in slope and hence may be used to identify grain boundaries and produce conventional height maps [74]. Thus, as shown by the solid double arrows in Fig. 12,  $v_j$  can be determined using the height map precisely at the grain boundaries which are identified using the amplitude error map. Due to the easy identification of the grain boundaries using this procedure, the large topographic contrast arising from the deformation of a ductile material to a very high strain does not prevent an unambiguous measurement of GBS. Accordingly, this method was successfully employed to measure GBS in UFG samples tested in tension to failure with accumulated total strains up to >70 % [62]. In practice, the profile for  $v_j$  as shown in Fig. 12 may be generated also from SEM micrographs of an FIB-milled trench in the deformed sample as shown in Fig. 10.

In addition to this direct method for measuring GBS, micro-indentation testing of the type shown in Fig. 9 followed by AFM analysis of the topography of the material pileup may be used also to quantitatively determine the role of GBS in the deformation of UFG materials [47, 48]. Furthermore, the magnitude of GBS can be ascertained, at least qualitatively, by using orientation image mapping [75] or micro-texture analysis [76]. Thus, a displacement in

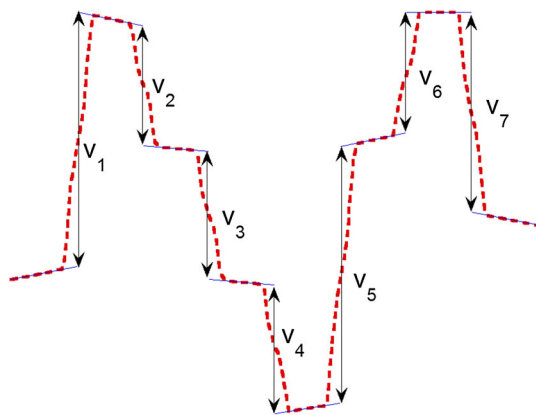


**Fig. 12** A schematic illustration of the surface topographic profile of a deformed sample of the Al–7 % Si alloy as determined using an AFM scan: the *dashed line* represents the actual profile, the *solid lines* are best fits to the profiles of the grains, and the vertical offsets  $v_j$  are determined at the points marked by the vertical *double arrows* [62]

the relative locations of neighboring grains in grain orientation maps acquired before and after the deformation provides a direct confirmation of the occurrence of GBS [75] and similarly a decrease in the maximum texture intensity following deformation also qualitatively demonstrates the occurrence of GBS [76].

### The implication of GBS in UFG materials at low temperatures

As shown in Figs. 4 and 5, the processing of an Al–7 % Si alloy by HPT reveals a clear transition from conventional behavior to the HSHD region with the imposition of additional strain. Concurrently, there was also a measured increase in the strain rate sensitivity from  $\sim 0.02$  in the conventional region to  $\sim 0.12$ – $0.14$  in the HSHD region [35, 62]. Furthermore, the samples falling within the HSHD region registered a moderate contribution of GBS ( $\xi \approx 15$ – $20$  %) whereas the samples exhibiting conventional behavior showed negligible GBS [62]. These observations directly relate the increase in the strain rate sensitivity to the enhanced occurrence of GBS and they unambiguously establish the significant role of GBS in achieving high ductilities at low temperatures and in promoting the transition from conventional behavior to the HSHD region.

There is also another important implication associated with the occurrence of GBS at low temperatures in UFG materials. Figure 13 shows the result of compression testing of a miniaturized sample of an Al–30 % Zn alloy, prepared in the form of a micro-pillar from an HPT disk, where the compression was conducted at room temperature using a depth-sensing ultra-microhardness testing facility and the grain size of the material was in the range of  $\sim 200$ – $400$  nm [77, 78]. Due to the very limited number of grains that are generally available in micro-pillars prepared from conventional CG materials, they invariably suffer from strain avalanches which arise due to the occurrence of complex and intermittent dislocation slip events [79–83]. By contrast, and as is evident from the protrusion of multiple grains in Fig. 13, the micro-pillar of this SPD-processed UFG material comprises multiple grains across the diameter and height of the sample and this leads to significant GBS so that the deformation field in the micro-pillar becomes uniform and the stress–strain curve is smooth and free of any strain avalanches [77, 78]. Furthermore, UFG micro-pillars of this type also show higher strain hardening and a higher strain rate sensitivity compared to micro-pillars of the conventional CG alloy [77]. This remarkable result attests to the overall homogeneity of the deformation and accordingly to the potential for making use of these materials in micro-devices.

The experimental results described in this section firmly establish that, due to the unique features of the grain

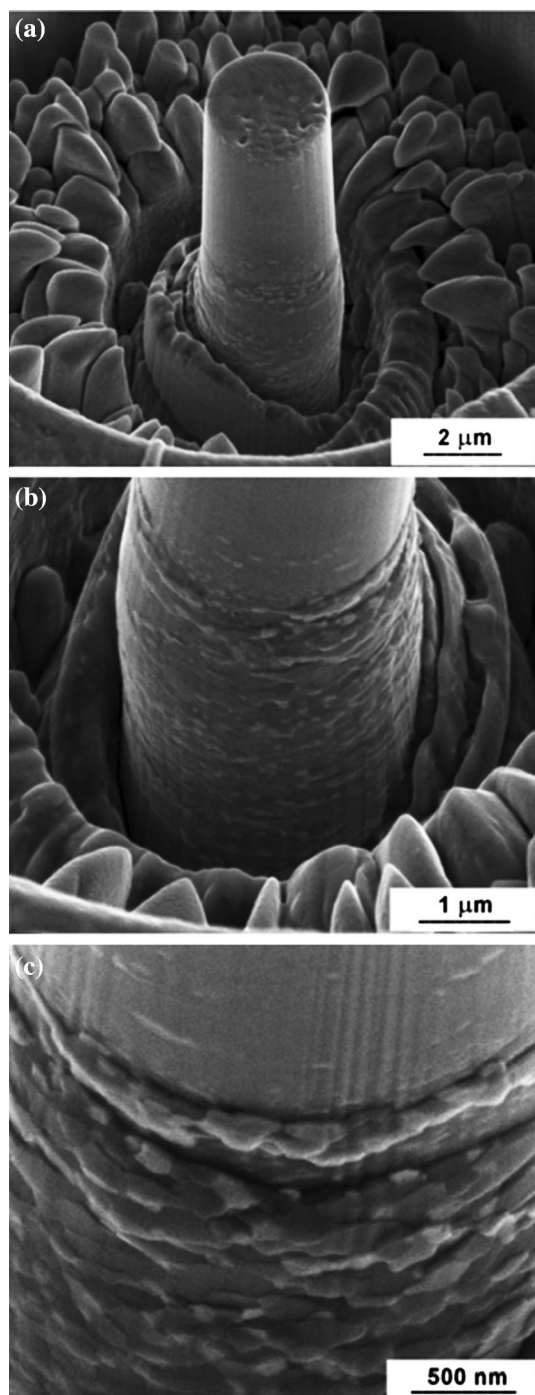


**Fig. 13** A micro-pillar sample of a UFG Al–30 % Zn alloy after HPT and compression testing at **a** low, **b** intermediate and **c** high magnifications: the sample was processed through five turns of HPT giving a grain size of  $\sim 200\text{--}400$  nm [77]

boundaries in SPD-processed UFG materials, GBS occurs even at temperatures which are exceptionally low by conventional standards. Furthermore, due to the unique combination of Hall–Petch strengthening as described by Eq. (1) and the enhanced ductilities that are a direct

consequence of the occurrence of GBS at low temperatures, it is readily concluded that continued processing by SPD to high strains provides a simple procedure for simultaneously achieving both high strength and high ductility in these UFG materials.

### Summary and conclusions

- (1) Ultrafine-grained materials may be prepared through the application of severe plastic deformation to bulk solids but testing at low temperatures shows these materials generally have high strength but only limited ductility.
- (2) There is experimental evidence demonstrating that it is often possible to achieve both high strength and high ductility by processing the material by SPD to a very high strain and/or by giving the material a short-term anneal immediately after processing.
- (3) The development of reasonable ductility is attributed to the occurrence of grain boundary sliding. Sliding is a possible deformation mechanism even at these relatively low temperatures because of the presence of a large volume of non-equilibrium grain boundaries exhibiting enhanced diffusivity.

**Acknowledgements** This work was supported in part by IISc-STC grant # ISTC0305 and a Seed Grant (Indian Institute of Science, Bangalore) to PK, in part by the NRF Korea funded by MoE under Grant No. NRF-2014R1A1A2057697 to MK and in part by the National Science Foundation of the United States under Grant No. DMR-1160966 and the European Research Council under ERC Grant Agreement No. 267464-SPDMETALS to TGL.

**Conflict of interest** The authors declare that they have no conflict of interest.

### References

1. Hall EO (1951) The deformation and ageing of mild steel: III discussion of results. *Proc Phys Soc B* 64:747–753
2. Petch NJ (1953) The cleavage strength of polycrystals. *J Iron Steel Inst* 173:25–28
3. Valiev RZ, Kaibyshev OA, Kuznetsov RI, Musalimov RSh, Tsenev NK (1988) Low-temperature superplasticity of metallic materials. *Dokl Akad Nauk SSSR* 301:864–866
4. Valiev RZ, Islamgaliev RK, Alexandrov IV (2000) Bulk nanostructured materials from severe plastic deformation. *Prog Mater Sci* 45:103–189
5. Valiev RZ, Estrin Y, Horita Z, Langdon TG, Zehetbauer MJ, Zhu YT (2006) Producing bulk ultrafine-grained materials by severe plastic deformation. *JOM* 58(4):33–39
6. Alexander DJ (2007) New methods for severe plastic deformation processing. *J Mater Eng Perform* 16:360–374
7. Zhu Y, Valiev RZ, Langdon TG, Tsuji N, Lu K (2010) Processing of nanostructured metals and alloys via plastic deformation. *MRS Bull* 35:977–981

8. Estrin Y, Vinogradov A (2013) Extreme grain refinement by severe plastic deformation: a wealth of challenging science. *Acta Mater* 61:782–817
9. Langdon TG (2013) Twenty-five years of ultrafine-grained materials: achieving exceptional properties through grain refinement. *Acta Mater* 61:7035–7059
10. Huang Y, Langdon TG (2013) Advances in ultrafine-grained materials. *Mater Today* 16:85–93
11. Kawasaki M, Langdon TG (2014) Producing ultrafine-grained materials through severe plastic deformation. *Emerging Mater Res* 3:252–260
12. Zhilyaev AP, Kim BK, Nurislamova GV, Baró MD, Szpunar JA, Langdon TG (2002) Orientation imaging microscopy of ultrafine-grained nickel. *Scripta Mater* 46:575–580
13. Zhilyaev AP, Nurislamova GV, Kim BK, Baró MD, Szpunar JA, Langdon TG (2003) Experimental parameters influencing grain refinement and microstructural evolution during high-pressure torsion. *Acta Mater* 51:753–765
14. Wongsangam J, Kawasaki M, Langdon TG (2013) A comparison of microstructures and mechanical properties in a Cu–Zr alloy processed using different SPD techniques. *J Mater Sci* 48:4653–4660. doi:10.1007/s10853-012-7072-0
15. Valiev RZ, Langdon TG (2006) Principles of equal-channel angular pressing as a processing tool for grain refinement. *Prog Mater Sci* 51:881–981
16. Zhilyaev AP, Langdon TG (2008) Using high-pressure torsion for metal processing: fundamentals and applications. *Prog Mater Sci* 53:893–979
17. Valiev RZ, Alexandrov IV, Zhu YT, Lowe TC (2002) Paradox of strength and ductility in metals processed by severe plastic deformation. *J Mater Res* 17:5–8
18. Valiev R (2002) Materials science - Nanomaterial advantage. *Nature* 419:887–889
19. Valiev R (2004) Nanostructuring of metals by severe plastic deformation for advanced properties. *Nat Mater* 3:511–516
20. Jia D, Wang YM, Ramesh KT, Ma E, Zhu YT, Valiev RZ (2001) Deformation behavior and plastic instabilities of ultrafine-grained titanium. *Appl Phys Lett* 79:611–613
21. Wang YM, Ma E (2004) Strain hardening, strain rate sensitivity, and ductility of nanostructured metals. *Mater Sci Eng A* 375–377:46–52
22. Zhu YT, Liao X (2004) Retaining ductility. *Nat Mater* 3:351–352
23. Wang Y, Chen M, Zhou F, Ma E (2002) High tensile ductility in a nanostructured metal. *Nature* 419:912–915
24. Wang YM, Ma E (2004) Three strategies to achieve uniform tensile deformation in a nanostructured metal. *Acta Mater* 52:1699–1709
25. Horita Z, Ohashi K, Fujita T, Kaneko K, Langdon TG (2005) Achieving high strength and high ductility in precipitation-hardened alloys. *Adv Mater* 17:1599–1602
26. Zhao YH, Liao XZ, Cheng S, Ma E, Zhu YT (2006) Simultaneously increasing the ductility and strength of nanostructured alloys. *Adv Mater* 18:2280–2283
27. Zhao YH, Bingert JE, Liao XZ, Cui BZ, Han K, Sergueeva AV, Mukherjee AK, Valiev RZ, Langdon TG, Zhu YTT (2006) Simultaneously increasing the ductility and strength of ultra-fine-grained pure copper. *Adv Mater* 18:2949–2953
28. Ma E (2006) Eight routes to improve the tensile ductility of bulk nanostructured metals and alloys. *JOM* 58(4):49–53
29. Zhao YH, Bingert JF, Zhu YT, Liao XZ, Valiev RZ, Horita Z, Langdon TG, Zhou YZ, Lavernia EJ (2008) Tougher ultrafine grain Cu via high-angle grain boundaries and low dislocation density. *Appl Phys Lett* 92:081903
30. Zhao YH, Topping T, Bingert JF, Thornton JJ, Dangelewicz AM, Li Y, Liu W, Zhu YT, Zhou Y, Lavernia EJ (2008) High tensile ductility and strength in bulk nanostructured nickel. *Adv Mater* 20:3033
31. Zhao Y, Zhu Y, Lavernia EJ (2010) Strategies for improving tensile ductility of bulk nanostructured materials. *Adv Eng Mater* 12:769–778
32. Huang CX, Hu WP, Wang QY, Wang C, Yang G, Zhu YT (2015) An ideal ultrafine-grained structure for high strength and high ductility. *Mater Res Lett* 3:88–94
33. Zhao YH, Guo YZ, Wei A, Dangelewicz AM, Xu C, Zhu YT, Langdon TG, Zhou YZ, Lavernia EJ (2008) Influence of specimen dimensions on the tensile behavior of ultrafine-grained Cu. *Scripta Mater* 59:627–630
34. Zhao YH, Guo YZ, Wei Q, Topping TD, Dangelewicz AM, Zhu YT, Langdon TG, Lavernia EJ (2009) Influence of specimen dimensions and strain measurement methods on tensile stress-strain curves. *Mater Sci Eng* 525A:68–77
35. Mungole T, Kumar P, Kawasaki M, Langdon TG (2014) A critical examination of the paradox of strength and ductility in ultrafine-grained metals. *J Mater Res* 29:2534–2546
36. Valiev RZ, Sergueeva AV, Mukherjee AK (2003) The effect of annealing on tensile deformation behavior of nanostructured SPD titanium. *Scripta Mater* 49:669–674
37. Suo T, Li YI, Zhao F, Deng Q, Xie K (2011) Influence of short term annealing on strain hardening rate and flow stress of ultra-fine grained material processed by severe plastic deformation. *Mater Res Innov* 15(s1):S69–S72
38. Semenova I, Salimgareeva G, Da Costa G, Lefebvre W, Valiev R (2010) Enhanced strength and ductility of ultrafine-grained Ti processed by severe plastic deformation. *Adv Eng Mater* 12:803–807
39. Polyakov AV, Semenova IP, Valiev RZ, Huang Y, Langdon TG (2013) Influencing of annealing on ductility of ultrafine-grained titanium processed by equal-channel angular pressing-Conform and drawing. *MRS Commun* 3:249–253
40. Maury N, Zhang NX, Huang Y, Zhilyaev AP, Langdon TG (2015) A critical examination of pure tantalum processed by high-pressure torsion. *Mater Sci Eng A* 638:174–182
41. Andreau O, Gubicza J, Zhang NX, Huang Y, Jenei P, Langdon TG (2014) Effect of short-term annealing on the microstructures and flow properties of an Al–1% Mg alloy processed by high-pressure torsion. *Mater Sci Eng A* 615:231–239
42. Kumar P, Xu C, Langdon TG (2009) Influence of strain rate on strength and ductility in an aluminum alloy processed by equal-channel angular pressing. *J Mater Sci* 44:3913–3916. doi:10.1007/s10853-009-3535-3
43. Gifkins RC, Langdon TG (1965) On the question of low-temperature sliding at grain boundaries. *J Inst Metals* 93:347–352
44. Ashby MF, Raj R (1970) Diffusion controlled sliding at serrated grain boundary. *Scripta Metall* 4:737–742
45. Langdon TG (2006) Grain boundary sliding revisited: developments in sliding over four decades. *J Mater Sci* 41:597–609. doi:10.1007/s10853-006-6476-0
46. Kawasaki M, Langdon TG (2007) Principles of superplasticity in ultrafine-grained materials. *J Mater Sci* 42:1782–1796. doi:10.1007/s10853-006-0954-2
47. Chinh NQ, Szommer P, Csanádi T, Langdon TG (2006) Flow processes at low temperatures in ultrafine-grained aluminum. *Mater Sci Eng A* 434:326–344
48. Chinh NQ, Szommer P, Horita Z, Langdon TG (2006) Experimental evidence for grain-boundary sliding in ultrafine-grained aluminum processed by severe plastic deformation. *Adv Mater* 18:34–39
49. Ivanov KV, Naydenkin EV (2014) Tensile behavior and deformation mechanisms of ultrafine-grained aluminum processed using equal-channel angular pressing. *Mater Sci Eng A* 606:313–321

50. Ivanov KV, Naydenkin EV (2014) The effect of strain rate on tensile behavior and deformation mechanisms of ultrafine-grained aluminum. *IOP Conf Series. Mater Sci Eng* 63:012123
51. Van Swygenhoven H, Caro A (1997) Plastic behavior of nano-phase Ni: a molecular dynamics computer simulation. *Appl Phys Lett* 71:1652–1654
52. Schiötz J, Di Tolla FD, Jacobsen KW (1998) Softening of nanocrystalline metals at very small grain sizes. *Nature* 391:561–563
53. Van Swygenhoven H, Derlet PM (2001) Grain-boundary sliding in nanocrystalline FCC metals. *Phys Rev B* 64:224105
54. Valiev RZ, Gertsman VYu, Kaibyshev OA, Khannanov ShKh (1983) Non-equilibrium state and recovery of grain-boundary structure. 1. General analysis, crystallogometrical aspects. *Phys Stat Solidi (a)* 77:97–105
55. Valiev RZ, Korznikov AV, Mulyukov RR (1993) Structure and properties of ultrafine-grained materials produced by severe plastic deformation. *Mater Sci Eng A168*:141–148
56. Horita Z, Smith DJ, Furukawa M, Nemoto M, Valiev RZ, Langdon TG (1996) An investigation of grain boundaries in submicrometer-grained Al–Mg solid solution alloys using high-resolution electron microscopy. *J Mater Res* 11:1880–1890
57. Sauvage X, Wilde G, Divinski SV, Horita Z, Valiev RZ (2012) Grain boundaries in ultrafine grained materials processed by severe plastic deformation and related phenomenon. *Mater Sci Eng A540*:1–12
58. Wilde G, Ribbe J, Reglitz G, Wegner M, Rösner H, Estrin Y, Zehetbauer M, Setman D, Divinski S (2010) Plasticity and grain boundary diffusion at small grain sizes. *Adv Eng Mater* 12:758–764
59. Kolobov YR, Grabovetskaya GP, Ivanov MB, Zhilyaev AP, Valiev RZ (2001) Grain boundary diffusion characteristics of nanostructured nickel. *Scripta Mater* 44:873–878
60. Fujita T, Horita Z, Langdon TG (2002) Characteristics of diffusion in Al–Mg alloys with ultrafine grain sizes. *Phil Mag A82*:2249–2262
61. Wang ZB, Lu K, Wilde G, Divinski SV (2010) Interfacial diffusion in Cu with a gradient nanostructured surface layer. *Acta Mater* 58:2376–2386
62. Mungole T, Kumar P, Kawasaki M, Langdon TG (2015) The contribution of grain boundary sliding in tensile deformation of an ultrafine grained aluminum alloy having high strength and high ductility. *J Mater Sci* 50:3549–3561. doi:10.1007/s10853-015-8915-2
63. Bell RL, Graeme-Barber C, Langdon TG (1967) The contribution of grain boundary sliding to the overall strain of a polycrystal. *Trans Met Soc AIME* 239:1821–1824
64. Langdon TG (1972) The effect of surface configuration on grain boundary sliding. *Metall Trans* 3:797–801
65. Islamgaliev RK, Yunusova NF, Valiev RZ, Tsenev NK, Perevezentsev VN, Langdon TG (2003) Characteristics of superplasticity in an ultrafine-grained aluminum alloy processed by ECA pressing. *Scripta Mater* 49:467–472
66. Kumar P, Xu C, Langdon TG (2005) The significance of grain boundary sliding in the superplastic Zn–22% Al alloy after processing by ECAP. *Mater Sci Eng A411–412*:447–450
67. Huang Y, Langdon TG (2002) Characterization of deformation processes in a Zn–22% Al alloy using atomic force microscopy. *J Mater Sci* 37:4993–4998. doi:10.1023/A:1021071228521
68. Huang Y, Langdon TG (2003) Using atomic force microscopy to evaluate the development of mesoscopic shear planes in materials processed by severe plastic deformation. *Mater Sci Eng A358*:114–121
69. Han JH, Mohamed FA (2011) Quantitative measurements of grain boundary sliding in an ultrafine-grained Al alloy by atomic force microscopy. *Metall Mater Trans A42*:3969–3978
70. Langdon TG (1994) An evaluation of the strain contributed by grain boundary sliding in superplasticity. *Mater Sci Eng A174*:225–230
71. Clarisse L, Bataille A, Penneec Y, Crampon J, Duclos R (1999) Investigation of grain boundary sliding during superplastic deformation of a fine-grained alumina by atomic force microscopy. *Ceram Int* 25:389–394
72. Kini M, Chokshi AH (2010) The influence of titania on creep in superplastic zirconia. *J Am Ceram Soc* 93:1725–1731
73. Ghosh S, Chokshi AH (2014) Creep in nanocrystalline zirconia. *Scripta Mater* 86:13–16
74. Eaton P, West P (2010) *Atomic Force Microscopy*. Oxford University Press, Oxford
75. Yang K, Fecht HJ, Ivanisenko Y (2014) First direct in situ observation of grain boundary sliding in ultrafine grained noble metal. *Adv Eng Mater* 16:517–521
76. Roy S, Suwas S (2013) Deformation mechanism during superplastic testing of Ti–6Al–4 V–0.1B alloy. *Mater Sci Eng A574*:205–217
77. Chinh NQ, Györi T, Valiev RZ, Szommer P, Varga G, Havancsák K, Langdon TG (2012) Observations of unique plastic behavior in micro-pillars of an ultrafine-grained alloy. *MRS Commun* 2:75–78
78. Chinh NQ, Valiev RZ, Sauvage X, Varga G, Havancsák K, Kawasaki M, Straumal BB, Langdon TG (2014) Grain boundary phenomena in an ultrafine-grained Al–Zn alloy with improved mechanical behavior for micro-devices. *Adv Eng Mater* 16:1000–1009
79. Greer JR, Oliver WC, Nix WD (2005) Size dependence of mechanical properties of gold at the micron scale in the absence of strain gradients. *Acta Mater* 53:1821–1830
80. Greer JR, Nix WD (2006) Nanoscale gold pillars strengthened through dislocation starvation. *Phys Rev B* 73:245410
81. Ng KS, Ngan AHW (2008) Stochastic nature of plasticity of aluminum micro-pillars. *Acta Mater* 56:1712–1720
82. Shao S, Abdolrahim N, Bahr DF, Lin G, Zbib HM (2014) Stochastic effects in plasticity in small volumes. *Int J Plast* 52:117–132
83. Crosby T, Po G, Erel C, Ghoniem N (2015) The origin of strain avalanches in sub-micron plasticity of fcc metals. *Acta Mater* 89:123–132